White Rose Research Online

eprints@whiterose.ac.uk
https://eprints.whiterose.ac.uk
Universities of Leeds, Sheffield and York

Deposited via The University of Sheffield.

White Rose Research Online URL for this paper:
https://eprints.whiterose.ac.uk/id/eprint/244108/

Version: Published Version

Article:
Belov, S., Jelínek, P., Karlický, M. et al. (2026) Collective and individual oscillations of prominence threads excited by vortex shedding. Monthly Notices of the Royal Astronomical Society, 551 (1). stag1415. ISSN: 0035-8711

https://doi.org/10.1093/mnras/stag1415

Reuse
This article is distributed under the terms of the Creative Commons Attribution (CC BY) licence. This licence allows you to distribute, remix, tweak, and build upon the work, even commercially, as long as you credit the authors for the original work. More information and the full terms of the licence here: https://creativecommons.org/licenses/

Takedown
If you consider content in White Rose Research Online to be in breach of UK law, please notify us by emailing eprints@whiterose.ac.uk including the URL of the record and the reason for the withdrawal request.

UNIVERSITY OF LEEDS
University of Sheffield
UNIVERSITY of York

Monthly Notices of the ROYAL ASTRONOMICAL SOCIETY

MNRAS **551,** 1–11 (2026)
Advance Access publication 2026 July 27

https://doi.org/10.1093/mnras/stag1415

Collective and individual oscillations of prominence threads excited by vortex shedding

Sofya Belov [1]★ Petr Jelínek,[1] Marian Karlický[2] and Robert Erdélyi[3,4,5]

[1]*Department of Physics, Faculty of Science, University of South Bohemia, Branišovská 1760, České Budějovice CZ-370 05, Czech Republic*
[2]*Academy of Sciences of the Czech Republic, v.v.i., Astronomical Institute, Fričova 258, Ondřejov CZ-251 65, Czech Republic*
[3]*School of Mathematical and Physical Sciences, Solar Physics & Space Plasma Research Center (SP2RC), University of Sheffield, Hounsfield Road S3 7RH, UK*
[4]*Department of Astronomy, Eötvös Loránd University, Pázmány Péter sétány 1/A, H-1112 Budapest, Hungary*
[5]*Hungarian Solar Physics Foundation (HSPF), Gyula Bay Zoltán Solar Observatory (GSO), Petőfi tér 3, H-5700 Gyula, Hungary*

Accepted 2026 July 23. Received 2026 July 21; in original form 2026 April 15

ABSTRACT

We investigate transverse oscillations in solar prominence threads. Previous studies have proposed that such oscillations may be driven by vortex shedding. Although vortex shedding is well understood in hydrodynamics, its role under magnetohydrodynamic (MHD) conditions, such as those in the solar atmosphere, remains insufficiently explored. To better address this issue, we perform 3-dimensional MHD numerical simulations of prominence threads, modelled in 4 cases with 1, 2, 3, and 7 cylinders, anchored at their ends, i.e. line-tied, otherwise free to deform and oscillate at other parts, interacting with a plasma flow. These test studies enabled us to analyse both their oscillations and the associated flow patterns. We observe oscillatory motions with components both parallel and perpendicular to the plasma bulk motion, sometimes one-dimensional, and sometimes coupled. The associated periods differ between the components and depend on the configuration of the cylinders. Further, the oscillations of individual cylinders occur either in phase, in anti-phase, or with a time delay, depending on their configuration. In some cases, the perpendicular oscillations are caused by vortex shedding, and in some cases a Kármán vortex street is clearly observed.

Key words: MHD – turbulence – Sun: corona – Sun: filaments, prominences – Sun: oscillations.

1 INTRODUCTION

The presence of an inhomogeneously distributed magnetic field in the solar atmosphere makes its plasma complexly structured and leads to the formation of configurations that act as waveguides (B. Roberts 1981a, b; P. M. Edwin & B. Roberts 1982, 1983; R. Erdélyi & N. K. Zsámberger 2024). A large class of waves observable in the solar atmosphere is referred to as magnetohydrodynamic (MHD) waves (e.g. E. Priest 2014) – a term introduced by H. Alfvén (1946) to describe wave motion produced by the interaction between mechanical and electromagnetic phenomena in electrically conductive liquids.

An example of magnetic structures observable in the solar atmosphere are solar prominences (I. Arregui, R. Oliver & J. L. Ballester 2018), which are large bright cloud-like features that extend to more than 50 Mm above the solar limb, formed by matter originating from the chromosphere and therefore on the order of a hundred times denser and cooler than the solar corona, in which they are embedded (A. Ambastha 2003), composed by multiple threads (I. Arregui et al. 2018).

In these threads, the presence of oscillatory motions has been confirmed by observations. These oscillations have been interpreted in terms of MHD waves. Prominence threads can oscillate collectively but also individually, when individual threads or groups of threads oscillate with their own periods independently on the rest of the prominence (I. Arregui et al. 2018).

The sausage mode and the kink mode of MHD waves are the cases of a longitudinal and transverse wave, respectively, with the lowest azimuthal wavenumbers (D. B. Jess et al. 2015). Kink-mode oscillations, i.e. standing kink-mode waves, in coronal loops are an intensively studied dynamic phenomenon in the solar corona (J. Andries et al. 2009; M. S. Ruderman & R. Erdélyi 2009; V. M. Nakariakov et al. 2016; T. J. Wang 2016; V. M. Nakariakov et al. 2021). Apart from coronal loops, these oscillations have been observed in solar prominences (I. Arregui et al. 2018).

V. M. Nakariakov, M. J. Aschwanden & T. Van Doorsselaere (2009) have suggested the role of the phenomenon of vortex shedding (VS) in the excitation of kink-mode oscillations in the corona. This phenomenon, well known in hydrodynamics, occurs in the wake of a bluff body (Z. Hao et al. 2022) at a certain range of Reynolds numbers *Re* (J. H. Lienhard (1966) states the range $40 \leq Re \lesssim 3 \cdot 10^5$ and $Re \geq 3.5 \cdot 10^6$, noting uncertainty about the upper *Re* boundary, for flows across circular cylinders) and consists in the periodical formation and detaching of vortices behind the body alternately from each side (Z. Hao et al. 2022). The process might lead to the formation of a pattern of vortices

★ E-mail: belovs00@prf.jcu.cz

© The Author(s) 2026.
Published by Oxford University Press on behalf of Royal Astronomical Society. This is an Open Access article distributed under the terms of the Creative Commons Attribution License (https://creativecommons.org/licenses/by/4.0/), which permits unrestricted reuse, distribution, and reproduction in any medium, provided the original work is properly cited.

Downloaded from academic.oup.com/mnras/article/551/1/stag1415/8743706 by guest on 04 September 2026

of opposite sign of vorticity, alternating along the streamwise direction, known as a Kármán vortex street (KVS; P. Roushan & X. L. Wu 2005).

Occurrence of VS in the solar corona has been suggested by the observations presented in H. Lee, Y.-J. Moon & V. M. Nakariakov (2015) and T. Samanta, H. Tian & V. M. Nakariakov (2019) and numerical simulations presented in M. Gruszecki et al. (2010), P. Syntelis & P. Antolin (2019), K. Karampelas & T. Van Doorsselaere (2021), and P. Jelínek, S. Belov & M. Karlický (2022). However, to the best of our knowledge, a KVS in the solar corona was for the first time observed by H. Wei et al. (2023), specifically, in concurrence with a Kelvin–Helmholtz instability.

In the model proposed in V. M. Nakariakov et al. (2009), kink-mode oscillations are excited by VS as follows: plasma with the magnetic field parallel to a coronal loop is dragged in the vertical direction by upflow associated with a coronal mass ejection (CME). This causes a horizontal quasi-periodic force to act alternately on the right and left sides of the magnetic structure. This, in turn, causes horizontally polarized kink-mode oscillations of the magnetic structure. This mechanism is the most effective when the alternate force is in resonance with the natural frequency of the kink-mode oscillations of the magnetic structure.

Compared to the model used in our previous study (P. Jelínek et al. 2022), which was three-dimensional and represented a prominence by a single simple magnetic structure, the model used in this study has a more complex geometry and therefore is less idealized. Specifically, we consider several progressively more complex scenarios: a single prominence thread, a system of two horizontally arranged prominence threads, a system of three vertically arranged prominence threads, and finally a large-scale structure composed of seven prominence threads. This allows us to explore the dynamics of a solar prominence as of a multicomponent system in which individual threads oscillate both individually and collectivelly.

The paper is structured as follows: Section 2 introduces the governing equations, model, and its numerical implementation. Section 3 presents and discusses the results. Finally, Section 4 presents the conclusions.

2 MODEL AND METHOD

This paper follows on from our study presented in P. Jelínek et al. (2022). This study included a parametric study of VS around a single motionless cylinder with five different initial magnetic field values and a study of oscillations of a single cylinder anchored at its ends, i.e. line-tied, otherwise free to deform and oscillate at other parts, excited by VS.

2.1 Governing equations

In our numerical model, the plasma dynamics is described by the 3D, time-dependent ideal MHD equations in a Cartesian coordinate system. We use the following form, written in terms of the convective (Lagrangian) derivative (see e.g. J. P. H. Goedbloed & S. Poedts (2004)):

$$\frac{\mathrm{D}\,\rho}{\mathrm{D}\,t} = -\rho\nabla\cdot\mathbf{v}, \tag{1}$$

$$\rho\frac{\mathrm{D}\,\mathbf{v}}{\mathrm{D}\,t} = -\nabla p + \mathbf{j}\times\mathbf{B}, \tag{2}$$

$$\frac{\mathrm{D}\,\mathbf{B}}{\mathrm{D}\,t} = (\mathbf{B}\cdot\nabla)\mathbf{v}, \tag{3}$$

$$\frac{\mathrm{D}\,e}{\mathrm{D}\,t} = -\frac{p}{\rho}\nabla\cdot\mathbf{v}, \tag{4}$$

$$\nabla\cdot\mathbf{B} = 0, \tag{5}$$

where all the terms have their usual meaning. Gravitational acceleration is not considered in the model, as follows from equation (2). Also, fully ionized plasma was considered (and therefore the adiabatic coefficient was set as $\gamma = \frac{5}{3}$) with an average mass of ions $1.2m_\mathrm{p}$, typical for the solar corona.

Generally, the terms expressing the radiative losses, R_loss, thermal conduction, T_cond, and heating, H, should be added to the set of MHD equations. Because simulations are performed in an energetically closed model without any external sources, we assume that radiative losses and thermal conduction are fully compensated by the heating, H; in other words, $R_\mathrm{loss} + T_\mathrm{cond} + H = 0$ during the whole studied process.

2.2 Numerical implementation

The MHD equations are solved numerically by the LARE3D, which is well tested, parallel and open-source simulation code. LARE3D is a Lagrangian remap numerical code that implements a staggered grid and is second order accurate in space and time (T. Arber et al. 2001). The code uses the Lagrangian-remap method, splitting each timestep into a Lagrangian step followed by a remap step – the grid mesh follows the fluid flow and later it is remapped onto its original state, which (apart from the interpolation inaccuracies) does not affect the fluid variables and only transfers them to the cells of the remapped grid, see e.g. S. M. Griffies, A. Adcroft & R. W. Hallberg (2020). Van Leer gradient limiters are used in remapping (T. Arber et al. 2001).

Fig.1 illustrates the simulation boxes in the initial states of the simulations. For Cases #1 to #3, a box of size $(-3, 3) \times (-3, 3)$ Mm in the horizontal direction and $(0, 20)$ Mm in the vertical direction was used. It was covered by $360 \times 360 \times 1200$ grid points respectively. A wider box was used for Case #4: $(-3.6, 3.6)$ Mm in the x-direction, the other dimensions were the same as in the other cases, i.e. this box was covered by $432 \times 360 \times 1200$ grid points. For each case, the chosen number of grid points was enough to cover the modelled structures sufficiently.

In the numerical model, for both studied cases, we use open (free) boundary conditions in $x-$ and $z-$directions, allowing the fluid move freely and leave the simulation box without any significant reflections. In y-direction (direction of the magnetic field lines) we implemented periodic boundary conditions.

The periods of the oscillations as well as the VS period were estimated by using wavelet analysis. For the analysis of wave signal, we use the Morlet wavelet, which consists of a plane wave modulated by a Gaussian,

$$\Psi(t) = \pi^{-1/4}\exp(i\sigma t)\exp(-t^2/2), \tag{6}$$

where the parameter σ allows trade between time and frequency resolutions. Here we assumed the value of parameter $\sigma = 6$, as recommended by M. Farge (1992). The wave periods are estimated from the global wavelet spectrum as the most dominant period in this spectrum. More details about the wavelet method and its implementation can be found e.g. in M. Farge (1992) and C. Torrence & G. P. Compo (1998).

To visualize the simulation data, we used MATLAB (The MathWorks 2024).

Downloaded from academic.oup.com/mnras/article/551/1/stag1415/8743706 by guest on 04 September 2026

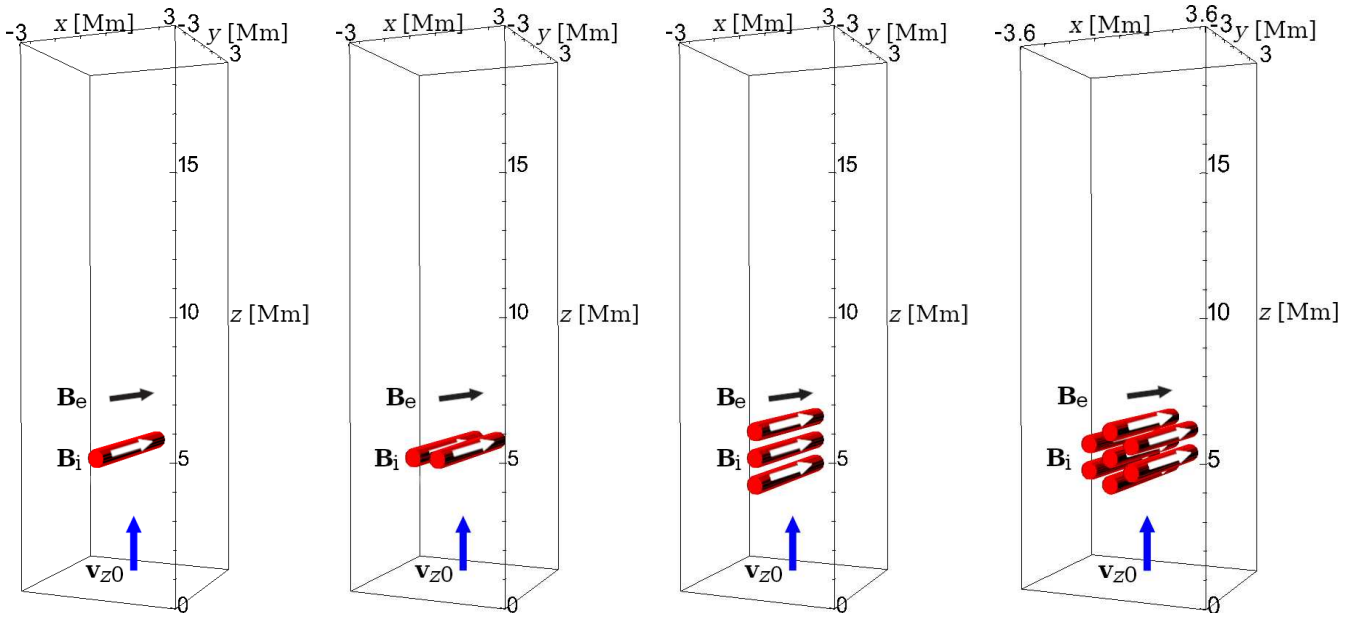


Figure 1. Sketches of the numerical boxes including their sizes. The cylinders represent the obstacles. The initial flow is denoted as $\mathbf{v}_{z0}$.

Table 1. Initial parameters of the studied cases – plasma flow velocity, external and cylinder magnetic fields, external and cylinder mass densities, external and cylinder temperatures, external, and cylinder plasma beta, respectively.

v_{z0} (m s^{-1})	$1.784 \cdot 10^5$
B_e (T)	10^{-3}
B_i (T)	$1.029 \cdot 10^{-3}$
ρ_e (kg m^{-3})	10^{-12}
ρ_i (kg m^{-3})	$5 \cdot 10^{-11}$
T_e (K)	$2 \cdot 10^6$
T_i (K)	$6 \cdot 10^3$
βe	0.069
β_i	0.010

2.3 Initial state

The parameters set in the initial conditions of each simulation are summarized in Table 1. All the initial parameters are in conformity with the equilibrium condition.

We consider four model cases: #1 – with one cylindrical obstacle free to deform and oscillate in all dimensions, with the radius square $r^2 = 0.1$ Mm^2, fixed at boundaries (in the cylinder parts close to the numerical box boundaries, namely for 2.75 Mm $< |y| \leq 3$ Mm, all plasma velocity components were fixed to zero throughout the simulations, which anchors the ends of the cylindrical structure. Therefore, since in our simulations the plasma dynamics is described by ideal MHD, the magnetic field remains also anchored, i.e. line-tied); #2 – two such bodies located next each other with the centres $2r$, $3r$, and $6r$ apart (a model with two cylindrical bodies was also used in the study of oscillations of coronal loops presented in M. Luna et al. 2008); #3 – three such bodies located above each other with the centres $3r$ apart; and #4 – with four more bodies added to the latter so that there is one central cylinder and six cylinders located around it in a circle, to achieve a higher refinement. Curvature and other complexity features of a prominence are not included in the model in order to avoid their simultaneous effects on the dynamics of the structure and the flow, which would be complicated to disentangle.

The length of the flexible part of a cylinder is 5.5 Mm. The magnetic field applied is aligned along the y-component of the initial axis of each cylinder. There is a constant flow coming from the lower boundary of the box throughout the simulations (although this plasma bulk motion was realized by a boundary condition at the lower boundary of the box, this motion is relative, i.e. the system is invariant under a reversal of the z-axis, because gravitation was not considered in our study. Therefore, it is possible to also treat the plasma bulk motion as the motion of the magnetic structure through a stationary plasma background). Its velocity corresponds to lower velocity values of CMEs. CME speeds are in the range $\sim$ 30-2600 km s^{-1}, with its average value throughout the solar cycle $\sim$ 428 km s^{-1} (S. Yashiro et al. 2004).

3 NUMERICAL RESULTS

In Figs 2, 4, 6, and 8, we approximately recorded the x- and z-components of the motion of the cylinders in all cases by locating the density-weighted centres of the area identified as the transverse cross-section of the cylinder at $y = 0$. The period values of both components of the oscillations, summarized in the following tables, were calculated using the data obtained by the method stated above.

Figs 3 , 5, 7, and 9 show the distribution of the mass density in the plane $y = 0$ in all cases. The colormaps are shown for different time steps, indicated above them. The entire evolution of mass density at $y = 0$ is shown in the movies attached to this paper.

3.1 Case #1

In Case #1, the cylinder undergoes decaying z-oscillations (i.e. vertically polarized) and deformations until $t \approx 200$ s, which can be seen in the corresponding movie, these oscillations are also evident from the right panel of Fig. 2. At $t \approx 280$ s, in the movie, we can see the beginning of VS leading to the creation of a KVS.

Downloaded from academic.oup.com/mnras/article/551/1/stag1415/8743706 by guest on 04 September 2026

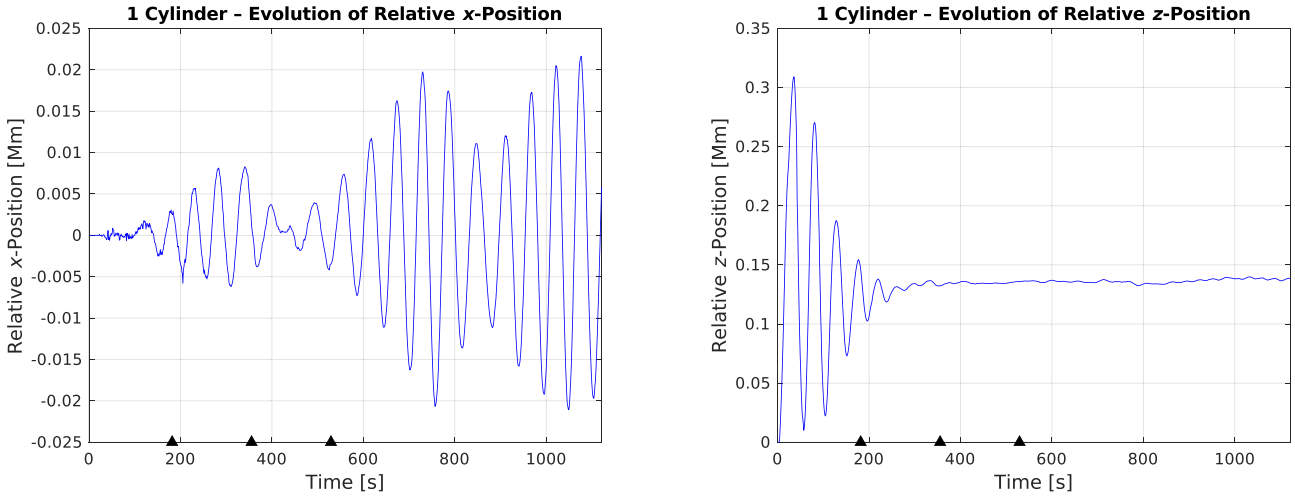


Figure 2. Left: evolution of relative x-position; right: evolution of relative z-position, i.e. displacement from initial positions, for Case #1. The marks indicate the time steps to which the relating mass density colormaps (Fig. 3) correspond.

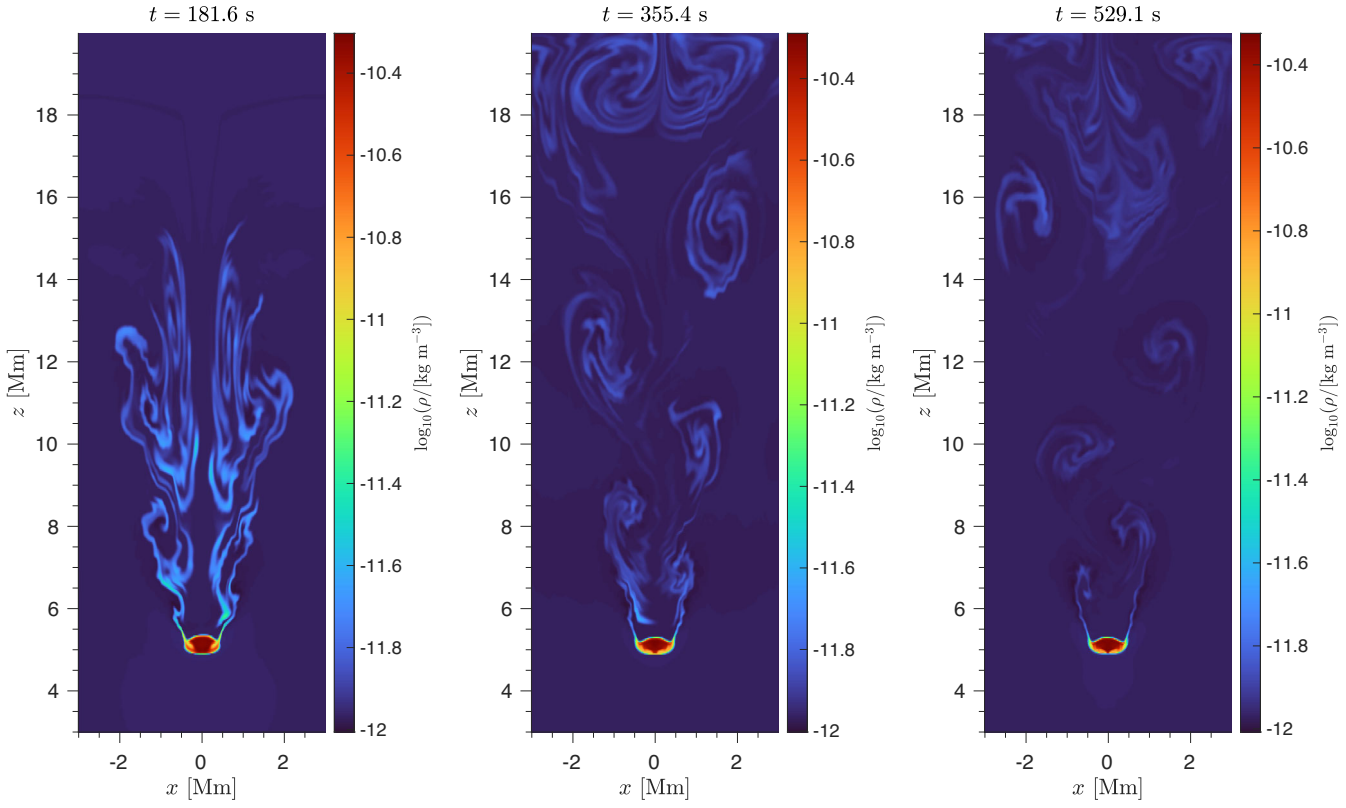


Figure 3. Mass density distribution in Case #1 at indicated time steps. In the middle and right panels, a KVS is captured.

A KVS is captured in the middle and right panels of Fig. 3. The structure of the vortices becomes more defined towards the end of the simulation. The evolution of the x-position of the density-weighted centre of the cylinder exhibits wave packet like behaviour – see left panel of Fig. 2. From $t \approx 700$ s, one may notice the appearance of low-amplitude x- (i.e. horizontally polarized) oscillations of the cylinder in the movie. The estimated period of the oscillation of the cylinder is 57.1 s for the x-direction (determined for interval 700.6-1121.0 s) and 49.1 s for the z-direction (determined for interval 0.0-195.1 s).

According to P. M. Edwin & B. Roberts (1983), a typical period of the kink mode of oscillation of a dense coronal loop is given by

$$P_{\rm kink} = \frac{2L}{C_{\rm kink}}, \tag{7}$$

where $L = \frac{\pi}{k}$, where k is the wavenumber, and for $C_{\rm kink}$, denoted as the'mean' Alfvénic speed of a kink mode, the following applies:

$$C_{\rm kink} = \sqrt{\frac{\rho_{\rm i} C_{\rm Ai}^2 + \rho_{\rm e} C_{\rm Ae}^2}{\rho_{\rm i} + \rho_{\rm e}}}, \tag{8}$$

Downloaded from academic.oup.com/mnras/article/551/1/stag1415/8743706 by guest on 04 September 2026

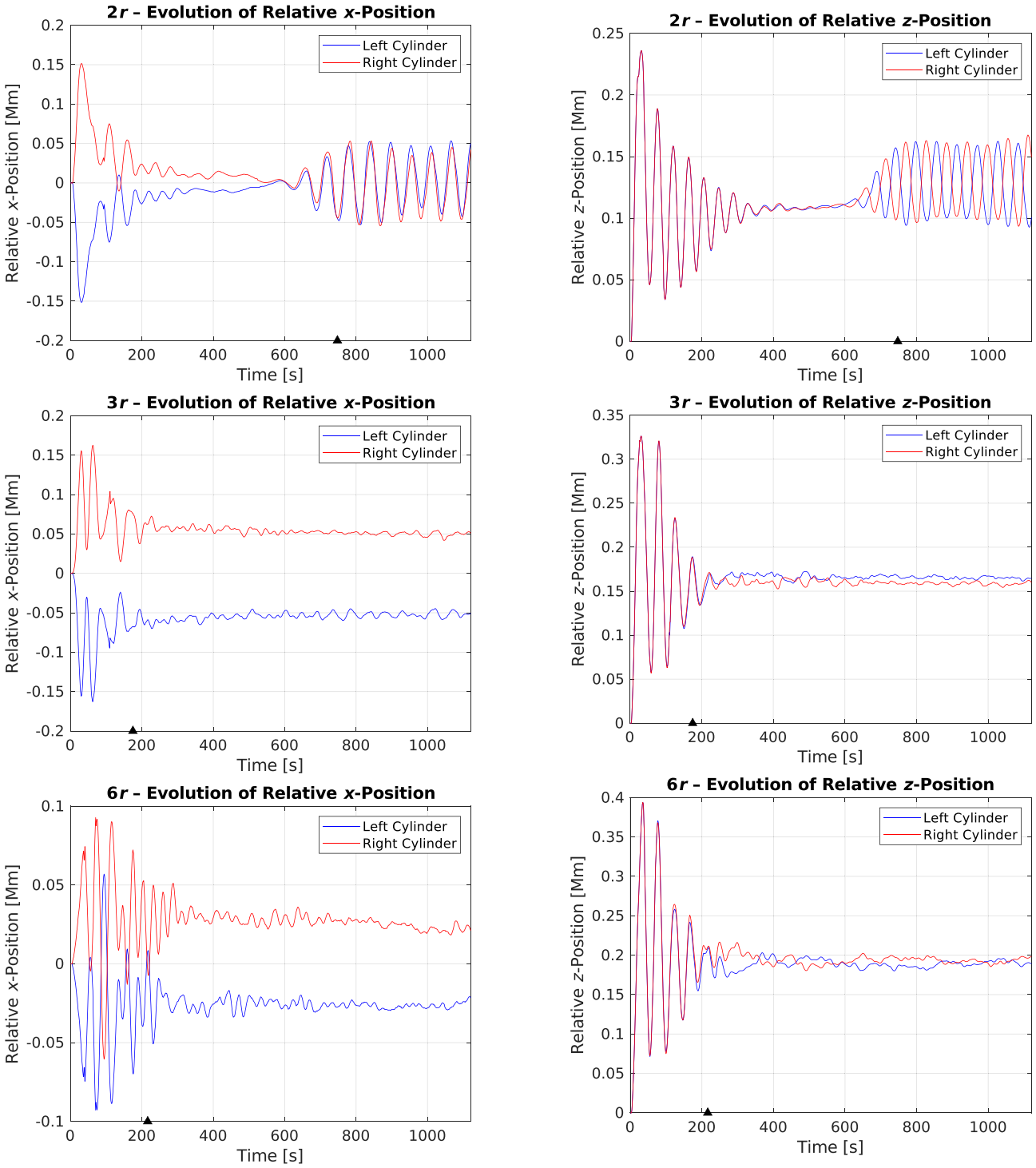


Figure 4. Comparison of the evolution of relative x-position (left panels) and z-position (right panels), i.e. displacement from initial positions, in Case #2 for different initial separations. The marks indicate the time-steps to which the relating mass density colormaps (Fig. 5) correspond.

where $\rho_{\rm i}$ and $\rho_{\rm ei}$ are the mass densities of the environment and the loop respectively, and $C_{\rm Ai}$ and $C_{\rm Ae}$ are the Alfvén speeds of the environment and the loop respectively. These relations are sometimes referred to as part of the so-called Zaitsev–Stepanov–Edwin–Roberts model (V. V. Zajtsev & A. V. Stepanov 1975), e.g. in V. M. Nakariakov et al. (2021). We used them for another estimation of the period value of the x-oscillations, which is presented below.

However, we note that these relations are derived within the linear approximation and for only free oscillation modes, while the oscillations considered in our study are forced (driven) with finite amplitudes. Also, in all studied cases, the cylinders exhibit

Downloaded from academic.oup.com/mnras/article/551/1/stag1415/8743706 by guest on 04 September 2026

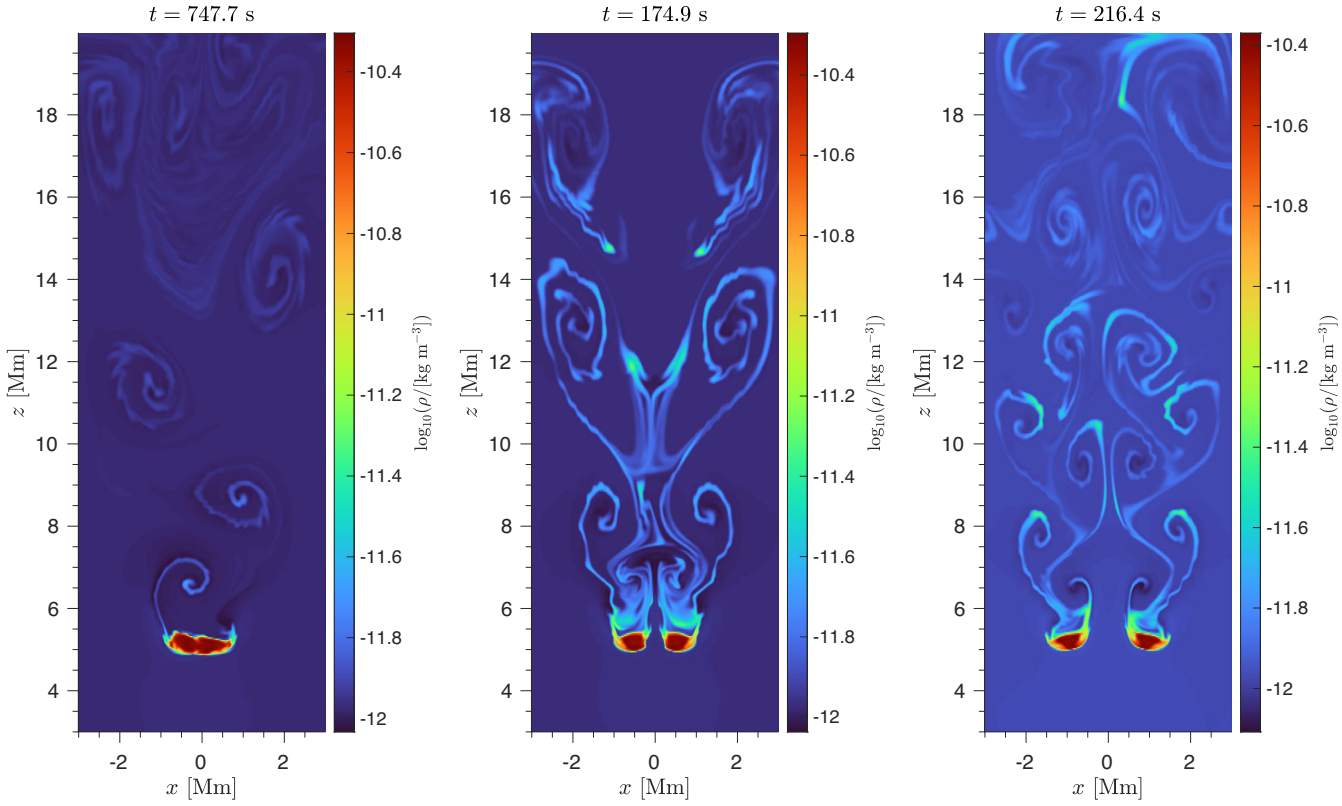


Figure 5. Mass density distribution in Case #2 for configurations 2*r*, 3*r*, and 6*r*, respectively, at indicated time-steps. In each case, VS is taking place – see movies. 2*r*: KVS is captured; 3*r*: two halves of KVSs are captured; 6r: two opposite KVSs are captured.

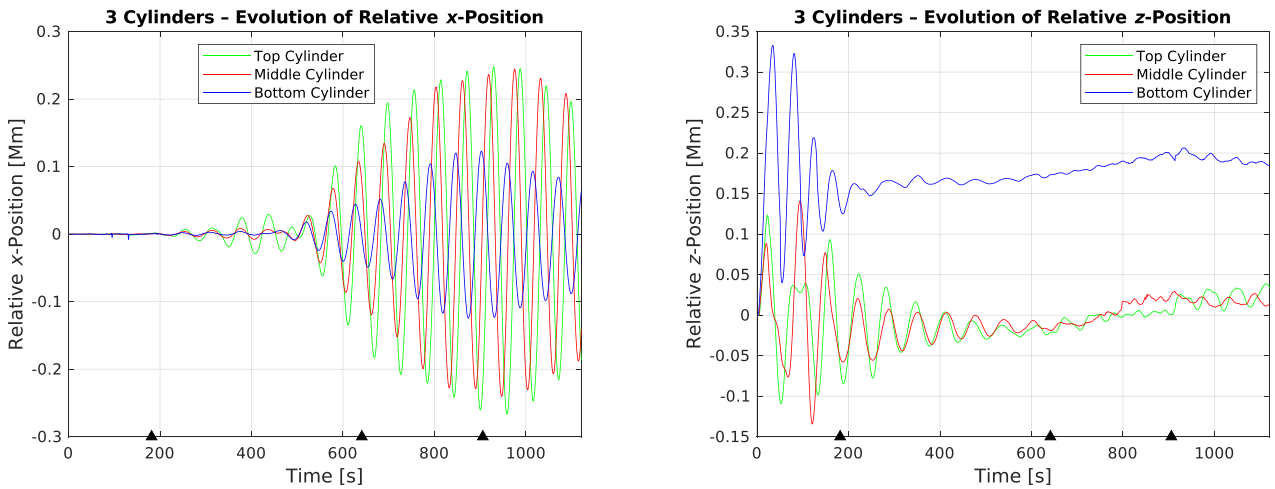


Figure 6. Left: evolution of relative *x*-position; right: evolution of relative *z*-position, i.e. displacement from initial positions, for Case #3. The marks indicate the time steps to which the relating mass density colormaps (Fig. 7) correspond.

different oscillation periods in the *x*- and *z*-directions. Therefore, a direct comparison between the period value estimated by the wavelet analysis and the period value estimated by equations (7) and (8) requires caution and may even be inaccurate.

In Case #1, the maximum amplitude of the *x*-oscillations (around 0.02 Mm) is significantly lower than the amplitude of the *z*-oscillations (around 0.3 Mm). This suggests that the *x*-oscillations are closer to free oscillations compared to the *z*-oscillations. Therefore, we used the latter two equations for an estimation of the period value of the *x*-oscillations.

The period of free oscillations according to these equations, calculated for the initial mass density values of our simulations, is 61.37 s. However, due to numerical diffusion across the cylinder's boundary, a slight reduction in mass density occurred during the simulation. This reduction in ρ_i non-negligibly influenced P_kink, leading to an estimated value of 59.85 s.

Downloaded from academic.oup.com/mnras/article/551/1/stag1415/8743706 by guest on 04 September 2026

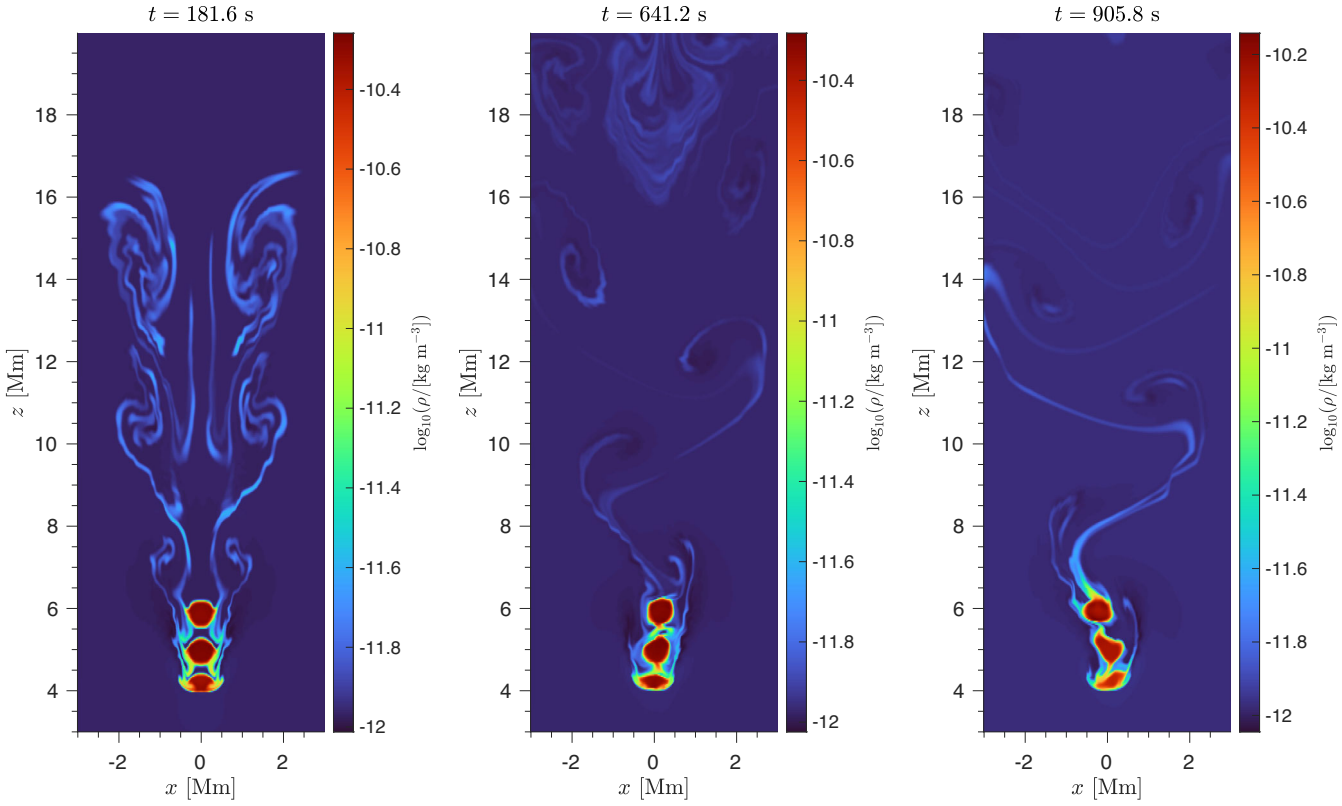


Figure 7. Mass density distribution in Case #3 at different time steps indicated above. In the middle panel, a KVS is well seen.

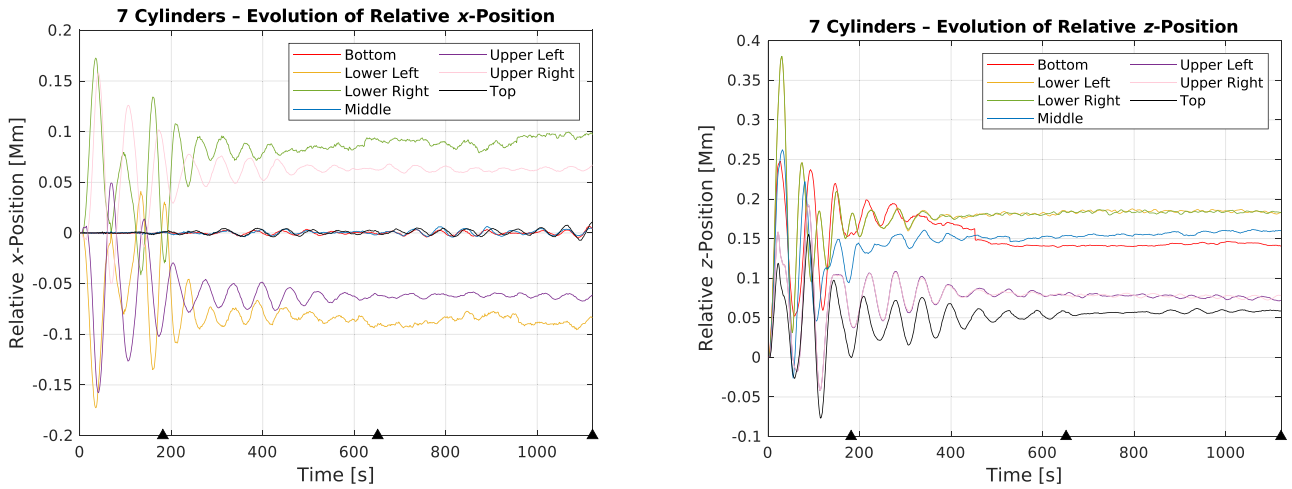


Figure 8. Left: evolution of relative x-position; right: evolution of relative z-position, i.e. displacement from initial positions, for Case #4. The marks indicate the time-steps to which the relating mass density colormaps (Fig. 9) correspond.

To reduce mass loss of the cylinder, we performed three test simulations of Case #1 with the radii of the fixed regions enlarged 1.05, 1.25, and 1.5 times. This enlarging led to lower mass-loss of the cylinder. At the same time, the period value of the x-oscillations obtained by the wavelet analysis changed: we obtained values 56.4, 50.5, and 52.7 s, respectively.

In the simulation without the fixed regions enlarged, the period value of the x-oscillations obtained by the wavelet analysis (57.1 s) approximates the value obtained by equations (7) and (8) more than in the simulations with the fixed regions enlarged. Also, enlarging the cross-sections of the fixed regions may lead to anchoring of magnetic field lines over a wider area. This increases the effective cross-section area of the cylinder, as shown by the fact that enlarging the radii of the fixed regions led to different oscillation periods. Thus, for all Cases #1 to #4, we decided to keep the setting without the enlarged fixed regions.

Downloaded from academic.oup.com/mnras/article/551/1/stag1415/8743706 by guest on 04 September 2026

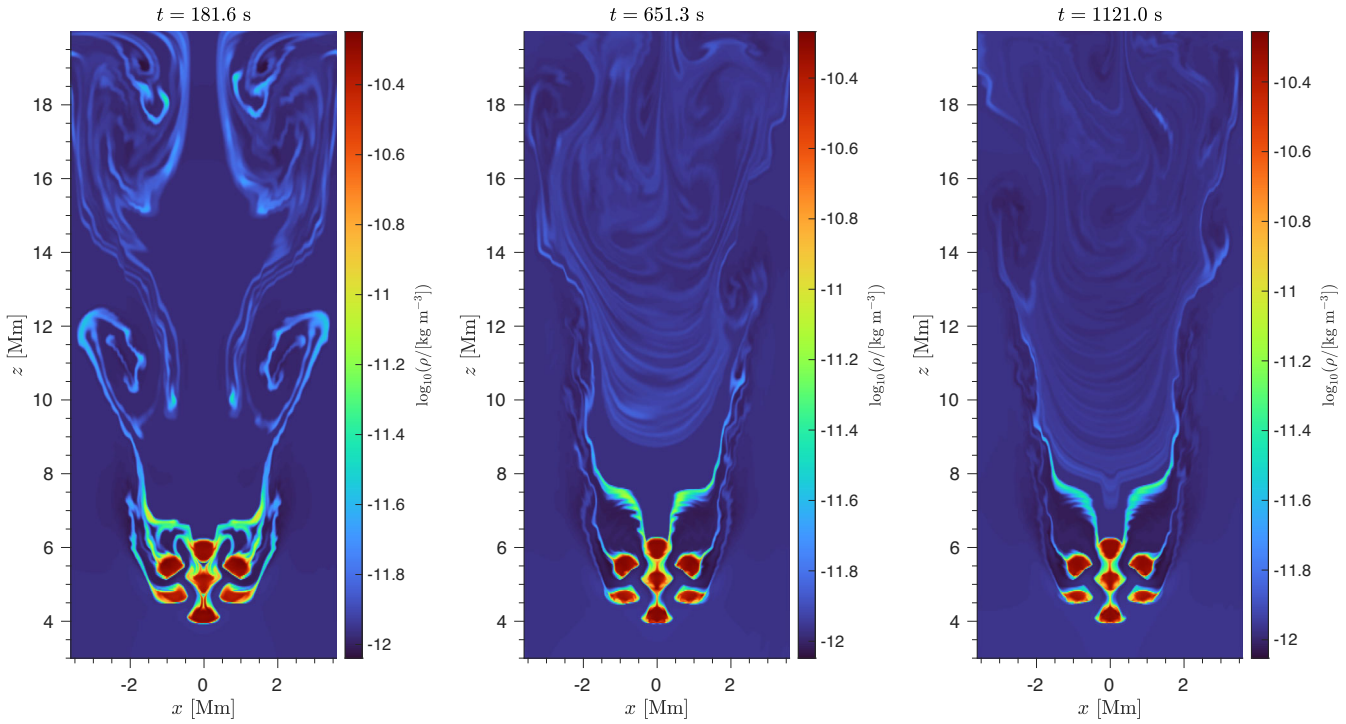


Figure 9. Mass density distribution in Case #4 at different time steps indicated above.

3.2 Case #2

In Case #2, in all the three simulations, the cylinders undergo decaying *xz* oscillations, i.e. oscillations with both *z*- (vertical) and *x*- (horizontal) components, and deformations in the beginning before becoming stabilized.

The left panels in Fig. 4, which correspond to the *x*-component of the motion, show slightly different but approximately symmetric motions (in anti-phase) of cylinders in each pair. The density-weighted centres of the cylinders in configurations 3*r* and 6*r* settle into small-amplitude fluctuations around mean *x*-positions with a separation distance larger compared to the initial distance between them; in the 3*r* configuration, they end up having moved away from each other by a greater distance. Compared to the 2*r* and 3*r* configurations, the 6*r* configuration leads to more numerous oscillations in the *x*-direction before the phase when the displacement of the density-weighted centres no longer shows pronounced extrema and only small irregular fluctuations around a mean value remain.

Regarding the evolution of the *z*-position, the cylinders settle into small-amplitude fluctuations around mean *z*-positions higher than the initial one; the greater the separation distance, the higher the resulting *z*-position. The 6*r* configuration leads to oscillations with the highest mean amplitude in the *z*-direction, and the 2*r* configuration leads to more numerous oscillations in the *z*-direction before the phase when the displacement of the density-weighted centres no longer shows pronounced extrema and only small irregular fluctuations around a mean value remain.

The estimated period values are summarized in Table 2. Surprisingly, the 3*r* configuration leads to the greatest period value of the decaying *z*-oscillations.

Table 2. Estimated period values of Case #2 determined by wavelet analysis. In the brackets, the time intervals for which the calculation was performed are stated.

	2*r*	3*r*	6*r*
z-direction	45.5 s (0.0-225.3 s)	49.1 s (0.0-149.1 s)	46.4 s (0.0-188.3 s)
	57.1 s (left)	–	–
	56.8 s (right)	–	–
	(713-1121.0 s)	–	–
x-direction	57.9 s (669.2-1121.0 s)	–	42.4 s (left), 42.7 s (right) (0.0-245.5 s)

For the 2*r* configuration, i.e. when the cylinders are in contact with each other, at $t \approx 330$ s, one may note how the symmetry of the wake starts considerably breaking, which is followed by VS, which leads to the creation of a single KVS – see left panel of Fig. 5, and later ($t \approx 690$ s) to kink mode oscillations, all persisting for the rest of the simulation (however, the vortices become less prominent). In the corresponding (upper) left panel in Fig. 4, the curves are approximately in anti-phase by $t \approx 600$ s, as the *x*-components of the motions of the density-weighted centres of the cylinders is towards to and away from each other, while later they are approximately in phase, which corresponds to the transitional motions of the pair as a whole. On the other hand, in the corresponding (upper) right panel in this figure, the curves overlap almost completely by $t \approx 600$ s, while later they are approximately in antiphase, which corresponds to small-angle rotational motions about the mid-point between the cylinders (while one cylinder goes up, the other goes down and vice versa).

Downloaded from academic.oup.com/mnras/article/551/1/stag1415/8743706 by guest on 04 September 2026

Table 3. Same parameters as in Table 2 for Case #3.

	Top	Middle	Bottom
z-direction	67.5 s	64.3 s	47.1 s
	(0.0-252.2 s)	(0.0-253.3 s)	(0.0-186.1 s)
x-direction	57.5 s	56.8 s	56.0 s
	(553.8-1121.0 s)	(549.3-1121.0 s)	(545.9-1121.0 s)

In case of the 3r configuration, we can shortly see VS past each cylinder before they stabilize (from $t \approx 120$ s to $t \approx 220$ s), however, it does not act as the trigger of the oscillations of the cylinders. Within this time interval, we can see something looking like two halves of opposite KVSs because the middle vortices do not contribute to the vortex chains – see middle panel of Fig. 5. After the stated approximate interval, the wakes of the cylinders are chaotic.

For the 6r configuration, similarly, we can see VS past each cylinder before they stabilize (from $t \approx 120$ s). This time, it leads to the formation of two KVSs persisting until $t \approx 280$ s, however, it does not act as the trigger of the oscillations of the cylinders. It is possible to see VS during the whole rest of the simulation, however, the vortices become much less prominent.

3.3 Case #3

In Case #3, vertically polarized oscillations and deformations of the cylinders are seen in the beginning of the corresponding movie too, initial oscillations are also seen in the right panel of Fig. 6; the bottom cylinder oscillates with the highest frequency. At $t \approx 350$ s the symmetry of the wake starts considerably breaking, then the flow oscillates and shortly after, VS leading to a KVS and later to horizontal oscillations of the cylinders takes place during the whole rest of the simulation. The x- (i.e. horizontally polarized) oscillations of this cylinder have the highest amplitude due to the influence of the vortices shed by its sides, while the x-oscillations of the bottom cylinder have the lowest amplitude, as seen in the movie and in the left panel of Fig. 6. The amplitude of the motions of the cylinders increases until a time-step not obvious from the movie. According to the left panel of Fig. 6, the x-oscillation amplitude decreases from $t \approx 931$ s for the bottom cylinder, from $t \approx 946$ s for the middle cylinder and from $t \approx 958$ s for the top cylinder. The higher the initial position of the cylinder, the highest the x-oscillation period. The calculated period values are summarized in Table 3. There is a phase shift between the motions of the cylinders visible from both the movie and Fig. 6 – the oscillation of the top cylinder lags behind the oscillation of the middle cylinder, and the oscillation of the middle cylinder lags behind the oscillation of the bottom cylinder. These lags increase over time due to the different period values.

3.4 Case #4

In Case #4, decaying z– (i.e. vertical) oscillations of the cylinders with the centres initially located at $x = 0$ and decaying xz-motions of the other cylinders are seen in Fig. 8. In the associated movie, one may also see their deformations. However, the symmetry of the wake does not break considerably; therefore, no VS takes place. The motions of the lateral cylinders in the x-direction are almost symmetrical within the upper and lower pairs, the lower lateral cylinders oscillate with a higher amplitude and settle into small-amplitude fluctuations around mean x-positions further from each other. Regarding the z-motions, the lower right and lower left cylinders oscillate with the highest amplitude in the beginning and settle into small-amplitude fluctuations around the highest z-position relative to the initial one, while the top cylinder does so around the lowest relative position.

Table 4. Period values of Case #4 calculated by the wavelet analysis. In the brackets, the time intervals for which the calculation was performed are stated.

	z-direction
Bottom	59.6 s
	(0.0–171.5 s)
Lower Left	45.5 s
	0.0–128.9 s)
Lower Right	45.8 s
	(0.0–127.8 s)
Middle	54.1 s
	(0.0–176.0 s)
Upper Left	59.2 s
	(0.0–186.1 s)
Upper Right	59.2 s
	(0.0–186.1 s)
Top	58.8 s
	(0.0–180.5 s)

The values of the periods of the z-component of the oscillations are stated in Table 4. The x-component of the motion exhibits oscillatory behaviour in the case of the lateral cylinders only. This is obvious from Fig. 8 (left panel), obtained by tracking the positions of their density-weighted centres, and was also verified by tracking the positions of their geometric centres. However, this behaviour is not apparent from the evolution of mass density distribution at $y = 0$ (see the corresponding movie), from which strong deformations of the structures in the corresponding time range are apparent. Therefore, the oscillatory behaviour of the x-component of the motion of the lateral cylinders, visible by tracking the density-weighted and geometric centres, reflect asymmetric deformation of the structures rather than coherent body displacement. For this reason, no period value was calculated for the x-component of the motion of these cylinders.

3.5 Comparison of oscillation periods

The period of the z-oscillations of the cylinder in Case #1 (49.1 s) differs by less than about 8 per cent from the periods of the z-oscillations of the cylinders in Case #2 (45.5, 49.1, and 46.4 s for configurations 2r, 3r, and 6r, respectively). This suggests that the presence of an identical neighbouring cylinder placed with the other one in a horizontal row does not substantially modify the dynamical conditions governing the oscillation.

The period of the z-oscillations of the bottom cylinder in Case #3 (47.1 s) differs from that of the cylinder in Case #1 (49.1 s) by about 4 per cent. In contrast, the middle and top cylinders of Case #3 show considerably greater periods of the z-oscillations (64.3 s and 67.5 s, respectively). This may be associated with the fact that the flow reaching these cylinders is modified by its interaction with the cylinder(s) below them. Moreover, the oscillation period increases with height within the whole vertical row.

Whenever VS led to the x-oscillations in a case of a group of cylinders, their period differed from the oscillation period of the cylinder in Case #1 during VS by around 2 per cent at most. In

Downloaded from academic.oup.com/mnras/article/551/1/stag1415/8743706 by guest on 04 September 2026

Case #3, in contrast to the z-oscillations, the obtained periods of the x-oscillations during VS remained within a narrow range: 56.0-57.5 s.

4 CONCLUSIONS

We present results of 3D ideal MHD numerical simulations of plasma flow interacting with single and multiple cylindrical structures representing prominence threads in the solar atmosphere. By systematically increasing the geometrical complexity of the system, we investigated how the arrangement of structures influences their oscillatory behaviour and the development of vortex shedding.

We studied the oscillations of a single cylindrical structure (Case #1), of two of them located next to each other with a variable separation distance (Case #2), of three of them located above each other (Case #3) and of six cylinders located in a circle around a central one (Case #4), each of them could move in all dimensions. In Cases #1 and #3, the cylinders exhibit initial oscillations that are only vertically polarized, as the lateral forces acting on the cylinders remain balanced during vertical displacement. In Cases #2 and #4, i.e. in the cases where horizontal structure is present, the cylinders exhibit initial oscillations with both z- (vertical) and x- (horizontal) components, as the presence of horizontally neighbouring cylinders does not let the mentioned horizontal balance be maintained during vertical displacement. The spatial configuration influences the amplitude, frequency and duration of these motions. Deformations of the cylinders are common to all simulations.

In the simulations of Cases #1, #2, and #3, in which the symmetry of the wake is sufficiently broken, VS leading to a KVS takes place. In the simulations of Cases #1 and #3, VS triggers sustained horizontal (kink mode) oscillations of them; in the simulation of Case #2 in which the cylinders are in contact (configuration 2r), VS triggers sustained oscillations with both x- and z-components. The estimated period values of these oscillations vary around 57 s.

In Case #1, the estimated period of the oscillation of the cylinder is 49.0 s for the vertical (z-) direction (in the beginning) and 57.1 s for the x-direction (during VS).

In the simulations of Case #2, the periods of the z-components of the initial oscillations are 45.5, 49.1, and 46.4 s for the configurations with separation distances between the cylinder centres 2r, 3r, and 6r (where r is the diameter of a cylinder), respectively. In the case of the configuration with separation distance 6r, which exhibited a sufficiently long initial oscillatory signal in the x-direction, the corresponding period was calculated as 42.4 and 42.7 s for the left and right cylinders, respectively.

In Case #2, for the configuration with separation distance 2r, i.e. when the cylinders are in contact, the VS led to oscillations of the cylinders. The flux tubes oscillated in both z- and x-directions. The calculated periods of the z-component of these oscillations are 57.1 and 56.8 s for the left and right cylinders, respectively. The calculated periods of the x-component are 57.9 s for both cylinders. During VS, they exhibit both antiphase and in-phase oscillations in the z- and x-directions, respectively.

The configuration of Case #3 leads to phase shifts and height-dependent oscillation periods. The calculated periods of the initial z-oscillations are 67.5, 64.6, and 47.1 s for the top, middle and bottom cylinders, respectively. The calculated periods of the following x-oscillations (during VS) are 57.5, 56.8, and 56.0 s for the top, middle and bottom cylinders, respectively. I.e. a higher distance from the flow source leads to a higher oscillation period.

In Case #4, the symmetry of the wake does not break significantly, therefore no VS takes place.

The simulation results suggest that vortex shedding is a possible mechanism for the excitation of kink mode oscillations of magnetic structures in the solar corona. However, as the stated above indicates, a horizontal separation between the magnetic structures can suppress coherent vortex-driven oscillations despite the presence of local vortex shedding. This highlights the importance of fine-scale structuring in determining the dynamical response of prominences.

Our results support the idea that vortex shedding may contribute to the excitation of transverse oscillations in solar prominences, particularly in multi-thread systems with favourable geometrical configurations. This mechanism may therefore play a role in the interpretation of observed prominence oscillations and in the broader context of coronal seismology.

ACKNOWLEDGEMENTS

The work in this paper is part of the project DynaSun. This project DynaSun has received funding under the Horizon Europe programme of the European Union under grant agreement (no. 101131534). Views and opinions expressed are, however, those of the author(s) only and do not necessarily reflect those of the European Union and therefore, the European Union cannot be held responsible for them.

This work was supported by the Ministry of Education, Youth and Sports of the Czech Republic through the e-INFRA CZ (ID:90254).

The authors acknowledge support from Grant 26–20555L of the Grant Agency of the Czech Republic.

RE is grateful to the Science and Technology Facilities Council (STFC, grant no. ST/M000826/1), UK. RE also acknowledges National Research, Development and Innovation Office (NKFIH; Hungarian Scientific Research Fund (OTKA), grant no. K142987 and Excellence Grant, grant no. TKP2021-NKTA-64), Hungary, and President's International Fellowship Initiative (PIFI, China, grant no. 2024PVA0043) for enabling this research.

The wavelet analysis was performed using the software written by C. Torrence and G. Compo, http://paos.colorado.edu/research/wavelets

DATA AVAILABILITY

The data underlying this article are available from the corresponding author on reasonable request.

REFERENCES

Alfvén H., 1946, Acta Radiologica, 27, 228
Ambastha A., 2003, in Antia H. M., Bhatnagar A., Ulmschneider P., eds, Vol. 619, Lectures on Solar Physics. Springer-Verlag, Berlin, Heidelberg, New York, p. 127
Andries J., Van Doorsselaere T., Roberts B., Verth G., Verwichte E., Erdélyi R., 2009, Space Sci. Rev., 149, 3
Arber T., Longbottom A., Gerrard C., Milne A., 2001, JCP, 171, 151
Arregui I., Oliver R., Ballester J. L., 2018, Living Rev. Sol. Phys., 15, 3
Edwin P. M., Roberts B., 1982, SoPh, 76, 239
Edwin P. M., Roberts B., 1983, SoPh, 88, 179
Erdélyi R., Zsámberger N. K., 2024, Symmetry, 16 1228
Farge M., 1992, AnRFM, 24, 395
Goedbloed J. P. H., Poedts S., 2004, Principles of Magnetohydrodynamics. Cambridge Univ. Press, Cambridge

Downloaded from academic.oup.com/mnras/article/551/1/stag1415/8743706 by guest on 04 September 2026

Griffies S. M., Adcroft A., Hallberg R. W., 2020, JAMES, 12, e2019MS001954
Gruszecki M., Nakariakov V. M., Van Doorsselaere T., Arber T. D., 2010, PRL, 105, 055004
Hao Z., Sun C., Lu Y., Bi K., Zhou T., 2022, Fluids, 7 194
Jelínek P., Belov S., Karlický M., 2022, ApJ, 941, 124
Jess D. B., Morton R. J., Verth G., Fedun V., Grant S. D. T., Giagkiozis I., 2015, Space Sci. Rev., 190, 103
Karampelas K., Van Doorsselaere T., 2021, ApJL, 908, L7
Lee H., Moon Y.-J., Nakariakov V. M., 2015, ApJL, 803, L7
Lienhard J. H., 1966, Bulletin 300, Synopsis of lift, drag, and vortex frequency data for rigid circular cylinders. Washington State University, College of Engineering, Research Division, Pullman, Washington
Luna M., Terradas J., Oliver R., Ballester J. L., 2008, ApJ, 676, 717
The MathWorks Inc., 2024, MATLAB. Natick, Massachusetts, USA. https://www.mathworks.com/products/matlab.html
Nakariakov V. M., Aschwanden M. J., Van Doorsselaere T., 2009, A&A, 502, 661
Nakariakov V. M. et al., 2016, Space Sci. Rev., 200, 75
Nakariakov V. M. et al., 2021, Space Sci. Rev., 217, 73
Priest E., 2014, Magnetohydrodynamics of the Sun. Cambridge Univ. Press, Cambridge
Roberts B., 1981a, SoPh, 69, 27
Roberts B., 1981b, SoPh, 69, 39
Roushan P., Wu X. L., 2005, Phys. Fluids, 17, 073601
Ruderman M. S., Erdélyi R., 2009, Space Sci. Rev., 149, 199
Samanta T., Tian H., Nakariakov V. M., 2019, PRL, 123, 035102
Syntelis P., Antolin P., 2019, ApJL, 884, L4
Torrence C., Compo G. P., 1998, BAMS, 79, 61
Wang T. J., 2016, Geophys. Monograph Ser., 216, 395
Wei H., Huang Z., Long D. M., Fu H., Xia L., Xiong M., Li B., 2023, A&A, 678, L7
Yashiro S., Gopalswamy N., Michalek G., St. Cyr O. C., Plunkett S. P., Rich N. B., Howard R. A., 2004, JGRA, 109, A07105
Zajtsev V. V., Stepanov A. V., 1975, IGAFS, 37, 3

SUPPLEMENTARY MATERIAL

Supplementary data are available at *MNRAS* online.

suppl_data

Please note: Oxford University Press is not responsible for the content or functionality of any supporting materials supplied by the authors. Any queries (other than missing material) should be directed to the corresponding author for the article.

This paper has been typeset from a TEX/LATEX file prepared by the author.

Downloaded from academic.oup.com/mnras/article/551/1/stag1415/8743706 by guest on 04 September 2026

© The Author(s) 2026.
Published by Oxford University Press on behalf of Royal Astronomical Society. This is an Open Access article distributed under the terms of the Creative Commons Attribution License (https://creativecommons.org/licenses/by/4.0/), which permits unrestricted reuse, distribution, and reproduction in any medium, provided the original work is properly cited.